


Rapid Hubble constant inference from GW170817 using GPU-accelerated nested sampling: prior sensitivity and the limits of post-hoc reweighting

Ming Han Yang ¹*, Metha Prathaban,^{2,3} David Yallup,^{4,2} and Will Handley^{4,2}

¹Independent researcher (formerly Institute of Astronomy and St John's College, University of Cambridge), UK

²Kavli Institute for Cosmology, University of Cambridge, Madingley Road, Cambridge CB3 0HA, UK

³Department of Physics, University of Cambridge, JJ Thomson Avenue, Cambridge CB3 0HE, UK

⁴Institute of Astronomy, University of Cambridge, Madingley Road, Cambridge CB3 0HA, UK

7 July 2026

ABSTRACT

The bright-siren measurement of the Hubble constant from GW170817 (Abbott et al. 2017b) assumes that switching from a volumetric to a uniform-in- d_L luminosity-distance prior can be implemented by post-hoc reweighting of the baseline samples, rather than by re-running the inference under the target prior. Using a GPU-native heterodyned nested sampling pipeline that completes the full $n_{\text{live}} = 5000$ analysis in ~ 13 min on a single A100, we recompute the GW170817 H_0 posterior under four prior variants for the modern aligned-spin tidal waveform IMRPhenomXAS_NRTidalv3. Switching from the volumetric to a uniform-in- d_L distance prior raises the high-tail probability $P(H_0 > 120 \text{ km s}^{-1} \text{ Mpc}^{-1})$ from 0.017 to 0.159 when imposed during sampling and shifts the weighted-median H_0 from 77.6 to 87.6 $\text{km s}^{-1} \text{ Mpc}^{-1}$, while the binned MAP stays at 70.5 $\text{km s}^{-1} \text{ Mpc}^{-1}$: both the tail and the bulk move under a change of prior that leaves the mode in place. Post-hoc reweighting of the baseline samples to the same target prior recovers only $P = 0.041$ in the tail, approximately 17% of the directly sampled shift. The three prior variants that carry an independent nested sampling evidence agree to $\Delta \ln Z \lesssim 1.8$, so the data show at most a weak preference among the distance priors; the tail and bulk shifts are therefore properties of the prior, not a data update. Targeted mode-isolated runs reveal a (d_L, ι) bimodality whose high- H_0 , low- d_L branch (Mode B; $|\ln \mathcal{B}_{B/A}| < 1$) the volumetric prior assigns negligible mass: this is the mechanism behind the reweighting deficit. The reweighted posterior has a lower effective sample size than the baseline, independently flagging the coverage failure. The runtime budget makes full-sample prior-sensitivity reruns the default robustness tool for bright-siren cosmology, replacing post-hoc reweighting.

Key words: gravitational waves – methods: data analysis – methods: statistical – stars: neutron – cosmological parameters – distance scale

1 INTRODUCTION

The present-day expansion rate of the Universe, quantified by the Hubble constant H_0 , is the subject of one of the most persistent tensions in contemporary cosmology. Measurements anchored in the early Universe, derived from observations of the Cosmic Microwave Background (CMB) assuming flat Λ CDM, favour a low value (Planck Collaboration 2020), while late-Universe distance ladder measurements based on Cepheids and Type Ia supernovae find a significantly higher value (Riess et al. 2016, 2022). The statistical and systematic discrepancy between these two families of measurement is now well established (Di Valentino et al. 2021), and its resolution – whether through unrecognised systematics or new cosmological physics – motivates independent probes of the expansion rate.

Gravitational-wave standard sirens are such a probe. The waveform amplitude of a compact-binary merger fixes the luminosity distance directly, without reference to an astrophysical distance ladder (Schutz 1986); Palmese & Mastrogiovanni (2025) review the methodology and its current status. When the merger is accompanied by an electro-

magnetic counterpart that identifies a host galaxy, the host redshift can be combined with the gravitational-wave distance to infer H_0 from a single event (Holz & Hughes 2005). The binary neutron-star merger GW170817 (Abbott et al. 2017a) is the canonical bright siren and the only confirmed example to date. Its uniqueness has motivated complementary galaxy-catalogue (dark-siren) analyses that infer the host redshift statistically rather than from a unique electromagnetic counterpart (LIGO Scientific Collaboration et al. 2026); the same scarcity of bright sirens makes careful treatment of the one we do have especially important. GW170817's association with the kilonova AT2017gfo in NGC 4993 yielded the first gravitational-wave H_0 measurement, $H_0 = 70_{-8}^{+12} \text{ km s}^{-1} \text{ Mpc}^{-1}$ at 68% credibility (Abbott et al. 2017b). That measurement has since been revisited from several directions: superluminal-jet constraints on the binary inclination (Mooley et al. 2018; Hotokezaka et al. 2019), improved peculiar-velocity modelling (Nicolaou et al. 2020; Mukherjee et al. 2021; Howlett & Davis 2020), and multi-wavelength afterglow analyses of GRB 170817A that constrain the viewing angle and shift H_0 towards the local distance-ladder value (Wang et al. 2023), most recently tightening the single-event result to $H_0 = 75.5_{-5.4}^{+5.3} \text{ km s}^{-1} \text{ Mpc}^{-1}$ at $\sim 7\%$ precision (Palmese et al. 2024). A parallel line of work has

* E-mail: mhy32@cantab.ac.uk

argued that residual binary-viewing-angle uncertainty contributes a $\gtrsim 10\%$ systematic on the GW170817 H_0 (Salvarese & Chen 2024); the prior-sensitivity question we address here sits in the same systematics-quantification programme.

For a single bright siren, the H_0 uncertainty is dominated by the luminosity–distance–inclination degeneracy: a face-on binary at larger d_L can produce the same observed strain as a more inclined binary at smaller d_L , with the two solutions mapping to different values of $H_0 \propto (v_r - v_p)/d_L$ for a fixed host recessional velocity v_r and peculiar velocity v_p . The resulting posterior is broad and skewed, and only weakly informative on H_0 from one event. In such a regime, the measurement is more sensitive to prior choices than the statistical uncertainty alone would suggest, because the prior shapes the tails of the posterior rather than just its peak. The original GW170817 analysis adopted a volumetric distance prior $\pi(d_L) \propto d_L^2$ over $[10, 75]$ Mpc and reported that switching to a flat-in-redshift prior (numerically \approx uniform-in- d_L at this redshift; see Section 2.4), implemented by *reweighting* posterior samples, left the bulk of the inferred H_0 posterior consistent with the volumetric baseline (their Extended Data Table 1; Abbott et al. 2017b). Whether the same conclusion holds when the prior is imposed during sampling rather than after the fact is the question this paper addresses.

Reweighting is attractive because it avoids rerunning expensive Bayesian inference. For a posterior $p(\theta | d, \pi_0)$ obtained under baseline prior π_0 , the target posterior under an alternative prior π_1 can be estimated by assigning each sample a weight proportional to $\pi_1(\theta)/\pi_0(\theta)$. This procedure is statistically consistent provided the baseline samples cover the support of the target posterior. If π_1/π_0 is large in regions that the baseline run has sampled sparsely, the reweighted estimator has high variance and systematically low tail mass (see e.g. Speagle 2020); Ashton (2026) gives a recent guide to reweighting gravitational-wave posteriors and its importance-sampling diagnostics. For GW170817, the baseline volumetric prior places little mass at low d_L ; a uniform-in- d_L target up-weights exactly this region, and the validity of reweighting is not obvious a priori.

Testing reweighting against a direct posterior obtained by sampling under the target prior requires repeated full gravitational-wave parameter estimation. In CPU frameworks such as BILBY (Ashton et al. 2019) and PARALLEL_BILBY, single-event binary-neutron-star analyses with phase-marginalised frequency-domain likelihood are sufficiently expensive that systematic exploration of distance, velocity, sampler, and waveform assumptions is rarely carried out in practice. Several recent developments make this constraint less severe: relative binning, also known as the heterodyned likelihood (Cornish 2010; Zackay et al. 2018), reduces the effective frequency grid for a long inspiral to a small number of bins; differentiable waveform libraries (Edwards et al. 2024) implemented in the JAX framework (Bradbury et al. 2018) enable end-to-end GPU evaluation of the likelihood; and accelerated nested sampling kernels, both CPU-side via normalising-flow proposals (Williams et al. 2021) and GPU-native via vectorised slice sampling (Cabezas et al. 2024; Yallup et al. 2026), retain the evidence estimates that nested sampling provides for free while permitting large live-point counts and repeated full reruns. Related accelerated binary-neutron-star pipelines (Krishna et al. 2023; Wong et al. 2023; Wouters et al. 2024) and forward-looking analyses (Hu & Veitch 2025) underscore the practical importance of compute-efficient parameter estimation for the third-generation detector era.

In this paper we use a GPU-native nested sampling pipeline – a BLACKJAX-NS slice-sampling kernel with a JAX implementation of the heterodyned likelihood – to revisit the GW170817 bright-siren H_0 inference of Abbott et al. (2017b). The inner kernel we adopt is the

GPU-native Nested Slice Sampling kernel of Yallup et al. (2026), implemented in the BLACKJAX-NS framework (Cabezas et al. 2024). The same framework was extended by Prathanan et al. (2026) to a GPU-native form of the BILBY “acceptance-walk” kernel, applied there to binary black hole events; the Nested Slice Sampling kernel itself was demonstrated on (short-duration, binary black hole) gravitational-wave signals in the brief conference note of Yallup et al. (2025). Here we apply the Nested Slice Sampling kernel at full production scale to a long-duration binary neutron star signal. Our focus is not a new single-event measurement of H_0 , but a controlled, multi-axis assessment of how that measurement depends on its priors, on the waveform, on the sampler hyperparameters, and on auxiliary inputs. We first validate the pipeline against GW150914 with the LVK GWTC-2.1+ production waveform IMRPhenomXPHM (Pratten et al. 2021; Abbott et al. 2024). We then report the IMRPhenomXAS_NRTidalv3 baseline GW170817 posterior, compare it with a direct uniform-in- d_L posterior and with the reweighted uniform-in- d_L posterior, and use targeted mode-isolated runs to identify the (d_L, t) bimodality that mechanistically explains the reweighting deficit. A waveform cross-check against TaylorF2 bounds the residual waveform systematic. Robustness sweeps over sampler hyperparameters, heterodyne-bin count, PSD source, heterodyne reference parameters, the host peculiar-velocity centre, and a companion IMRPhenomD_NRTidalv2 prior sweep are referenced in Appendix A. We finish by reporting heterodyne speedup and live-point scaling.

Section 2 describes the inference setup. Section 3 reports validation. Section 4 contains the prior-sensitivity analysis, the bimodality characterisation, and the waveform cross-check. Section 5 reports runtime and live-point scaling. Section 6 discusses implications and limitations. Section 7 concludes. Appendix A reports the inline robustness sweeps that are referenced in the body but not promoted to main figures.

2 METHOD

2.1 Nested sampling

For data d and source parameters θ under model \mathcal{M} , we target the posterior

$$p(\theta | d, \mathcal{M}) = \frac{\mathcal{L}(d | \theta, \mathcal{M}) \pi(\theta | \mathcal{M})}{Z(d | \mathcal{M})}, \quad (1)$$

where \mathcal{L} is the gravitational-wave likelihood, π the prior, and Z the Bayesian evidence. We estimate Z and draw posterior samples by nested sampling (Skilling 2006), using the Nested Slice Sampling implementation of Yallup et al. (2026) in the BLACKJAX-NS framework (Cabezas et al. 2024). The sampler evolves a population of live points through batched slice updates; this vectorisation keeps the GPU saturated when the per-evaluation likelihood cost is small.

All heterodyned GW170817 science runs reported here use $n_{\text{live}} = 5000$ live points, $n_{\text{delete}} = 2500$ points removed per iteration ($\frac{1}{2} n_{\text{live}}$), and $n_{\text{mcmc}} = 8 n_{\text{dim}} = 112$ slice-sampling steps per update, where n_{dim} is the dimensionality of the sampled parameter space (Table 1); runs terminate when the fractional evidence increment is below 10^{-3} . Scaling experiments vary n_{live} while holding all other settings fixed. The GW150914 IMRPhenomXPHM validation run uses the larger $n_{\text{live}} = 8000$, $n_{\text{delete}} = 2400$, $n_{\text{mcmc}} = 160$ ($16 n_{\text{dim}}$) configuration to verify that the validation conclusions are not sampler-limited at the smaller short-signal n_{dim} . A dedicated n_{mcmc} convergence sweep at $\{5, 10, 20\} \times n_{\text{dim}}$ for the 14-dimensional GW170817 problem is

Table 1. Nested sampling settings. n_{dim} is the sampled parameter-space dimension (14 for the phase-marginalised GW170817 runs, 10 for GW150914). Scaling experiments vary n_{live} with all other settings fixed.

Setting	GW170817	GW150914
n_{dim} (parameter dimension)	14	10
n_{live} (live points)	5000	8000
n_{delete} (removed per iteration)	2500	2400
n_{mcmc} (slice steps per update)	112	160
as a multiple of n_{dim}	$8 n_{\text{dim}}$	$16 n_{\text{dim}}$

left to follow-up work, with the headline tail probability $P(H_0 > 120 \text{ km s}^{-1} \text{ Mpc}^{-1})$ as the natural convergence diagnostic.

2.2 Heterodyned likelihood

The full frequency-domain likelihood for GW170817 uses 259 201 bins over 20–2048 Hz at $\Delta f = 1/128$ Hz for the 128 s strain segment. We use a heterodyned (relative-binning) likelihood (Cornish 2010; Zackay et al. 2018), in which the ratio between a candidate waveform and a reference waveform is approximated by a piecewise-linear function over a small set of coarse frequency bins; we use 501 nominal bins for GW170817 and 383 for GW150914. Other likelihood-compression schemes with different accuracy and setup trade-offs are available, notably reduced-order quadrature (Smith et al. 2016) and multibanding or adaptive frequency resolution (Vinciguerra et al. 2017; Morisaki 2021); we adopt relative binning for its simplicity and natural fit to a differentiable GPU likelihood. The reference waveform parameters and the per-waveform effective bin count after frequency-support masking are recorded in each run’s `config.json`. We compare heterodyned and full-resolution posteriors directly in Section 3.2 to verify that the approximation does not bias the source-parameter posterior at the level needed for H_0 inference.

All heterodyned runs analytically marginalise over the coalescence phase, so the sampled parameter space is fourteen-dimensional for GW170817 (intrinsic masses, aligned-spin z -components, tidal deformabilities, inclination, luminosity distance, coalescence time, polarisation angle, sky position, and the cosmological parameters H_0 and v_p), and ten-dimensional for GW150914.

2.3 Joint Hubble-constant likelihood

We sample the Hubble constant jointly with the gravitational-wave source parameters rather than post-processing the d_L marginal. The GW170817 host galaxy NGC 4993 contributes a CMB-frame recession velocity $v_r = 3327 \text{ km s}^{-1}$ with $\sigma_{v_r} = 72 \text{ km s}^{-1}$ and a Hubble-flow peculiar-velocity estimate $\langle v_p \rangle = 310 \text{ km s}^{-1}$ with $\sigma_{v_p} = 150 \text{ km s}^{-1}$. Both enter as Gaussian likelihood factors,

$$\begin{aligned} \ln \mathcal{L}_{\text{tot}}(\theta, H_0, v_p) = & \ln \mathcal{L}_{\text{GW}}(d | \theta) \\ & + \ln \mathcal{N}(v_r; H_0 d_L + v_p, \sigma_{v_r}) \\ & + \ln \mathcal{N}(\langle v_p \rangle; v_p, \sigma_{v_p}), \end{aligned} \quad (2)$$

following Abbott et al. (2017b). Equation 2 carries no $1/N_s(H_0)$ GW-detection selection factor because, for every prior variant considered in this work, $\pi(d_L | H_0)$ is independent of H_0 and the selection normalisation $N_s = \int P_{\text{det}}(d_L) \pi(d_L | H_0) dd_L$ is therefore an H_0 -independent constant that cancels from the joint posterior; we return to this point with the prior definitions in Section 2.4.

2.4 Priors and prior variants

The baseline prior configuration follows the bright-siren analysis of Abbott et al. (2017b): $\pi(d_L) \propto d_L^2$ over $[10, 75]$ Mpc, $\pi(H_0) \propto H_0^{-1}$ over $[45, 250]$ $\text{km s}^{-1} \text{ Mpc}^{-1}$, and $\pi(v_p) \propto 1$ over $[-1000, 1000]$ km s^{-1} combined with the Gaussian v_p -likelihood term in equation 2 at $\sigma_{v_p} = 150 \text{ km s}^{-1}$. The source-parameter priors reproduce those of the LVK GW170817 parameter estimation (Abbott et al. 2019a): the prior is uniform in the detector-frame component masses over $[0.5, 7.7] M_{\odot}$ with $m_1 \geq m_2$, subject to the additional chirp-mass constraint $1.184 \leq \mathcal{M}^{\text{det}} \leq 2.168 M_{\odot}$ (Abbott et al. 2019a, Sec. III D). As noted there, these bounds were chosen for technical reasons and the posterior has no support near them. The prior is full-sky, with right ascension uniform on $[0, 2\pi]$ and declination distributed according to a $\cos \delta$ prior on $[-\pi/2, \pi/2]$. Every heterodyned run reported here is full-sky.

We consider three prior variants in addition to the baseline:

- (i) *Direct uniform-in- d_L* : $\pi(d_L)$ uniform over the same fixed $[10, 75]$ Mpc window (independent of H_0), sampled directly.
- (ii) *Reweighted uniform-in- d_L* : the baseline posterior samples reweighted by the analytic ratio of the uniform-in- d_L to volumetric d_L priors.
- (iii) *Enlarged peculiar-velocity uncertainty*: identical to the baseline except $\sigma_{v_p} = 250 \text{ km s}^{-1}$.

The direct and reweighted uniform-in- d_L posteriors share the same target prior; they differ only in whether the prior is imposed during sampling or applied post-hoc. At GW170817’s source redshift ($z \lesssim 0.02$), the uniform-in- d_L prior is numerically equivalent within one per cent to the “flat-in-redshift” variant analysed by Abbott et al. (2017b) over the same distance range; we adopt the literal uniform-in- d_L form because it is what the inference pipeline imposes ($\pi(d_L)$ is a fixed density on the observable d_L , with no H_0 -dependent window). Consequently $\pi(d_L | H_0)$ has no H_0 -dependence for any of the three prior variants, so the GW-detection selection normalisation $N_s(H_0)$ of equation 2 is constant in H_0 and cancels from the joint posterior, exactly as for the volumetric baseline.¹

2.5 Waveforms

For GW170817 we adopt two waveforms in the main analysis, both evaluated with the JAX RIPPLE implementation (Edwards et al. 2024) within the JIM framework (Wong et al. 2023). The primary is IMRPhenomXAS_NRTidalv3, which combines the most recent NR-calibrated tidal-phase prescription (NRTidalv3; Abac et al. 2024) with a modern aligned-spin base (IMRPhenomXAS; Pratten et al. 2020); the differentiable JAX implementation we use is introduced in Chan et al. (2026).² TaylorF2 is included as a post-Newtonian inspiral-only family check, and we additionally analysed

¹ We verified this property by direct evaluation of $N_s(H_0) = \int P_{\text{det}}(d_L) \pi(d_L | H_0) dd_L$ over the LVK-matched $H_0 \in [45, 250]$ $\text{km s}^{-1} \text{ Mpc}^{-1}$ prior with a Finn–Chernoff antenna-pattern detection model (Finn & Chernoff 1993): N_s is H_0 -independent to machine precision for every horizon distance tested ($D_{\text{h}} \in \{100, 150, 220\}$ Mpc, spanning the published O2 BNS range to inspiral horizon; Abbott et al. 2020). The supporting calculation is in `analyze_selection_term.py` in the public repository.

² The IMRPhenomXAS_NRTidalv3 waveform is evaluated with R. Chan’s JAX reimplementations of the IMRPhenomX family in RIPPLE (<https://github.com/GW-JAX-Team/ripple>), used through the JIM framework (Wong et al. 2023) (<https://github.com/GW-JAX-Team/jim>); its fidelity against the

IMRPhenomD_NRTidalv2 as an anchor waveform for the IMRX-vs-NRTidalv2 capture-fraction comparison reported inline in Section 4.1; the JAX implementations of both tidal models were introduced in Wouters et al. (2024), and the corresponding full IMRPhenomD_NRTidalv2 posteriors are retained in the public test suite and summarised in Appendix A.

For GW150914 validation we use IMRPhenomXPHM (Pratten et al. 2021), the LVK GWTC-2.1+ production waveform for that event, which incorporates precession through a multi-scale-analysis treatment together with the dominant higher-order modes; we evaluate it with the JAX RIPPLe implementation (Edwards et al. 2024) within the JIM framework (Wong et al. 2023). Like-for-like comparison against the public LVK PE (Abbott et al. 2024; LIGO Scientific Collaboration & Virgo Collaboration 2022) therefore requires no waveform substitution.

2.6 Posterior summaries

We summarise one-dimensional marginals by a point estimate and a credible interval, both computed directly from the weighted posterior samples. The point estimate is the weighted-histogram mode, which we denote the maximum a posteriori (MAP) value: the centre of the maximum-weighted-count bin on a fixed $1 \text{ km s}^{-1} \text{ Mpc}^{-1}$ grid over $[40, 230] \text{ km s}^{-1} \text{ Mpc}^{-1}$. This is a posterior mode estimated from the sample set, not a likelihood maximisation; for the skewed uniform-in- d_L variants in Table 3 we additionally report the weighted posterior median (the interpolated 50th percentile of the weight-ordered cumulative distribution) as a bin-noise-robust complement. The credible intervals are highest-posterior-density (HPD) intervals – the shortest contiguous interval containing the requested cumulative weight – computed directly from the weighted samples at the stated credibility. All one-dimensional summaries – the MAP, the weighted median, the HPD intervals, and the tail probabilities $P(H_0 > 120 \text{ km s}^{-1} \text{ Mpc}^{-1})$ that carry the prior-sensitivity signal of Section 4.1 – are computed directly from the weighted samples with no kernel-density smoothing, so the reported tail statistics are not a smoothing artefact. The one-dimensional marginal curves displayed in Figures 3, 5 and 6 use a Silverman-bandwidth kernel-density estimate for visual presentation only; the quantitative tail comparisons never rely on them. Two-dimensional corner contours are likewise KDE-smoothed.

3 VALIDATION

3.1 GW150914

We validate the pipeline on the binary-black-hole event GW150914 (Abbott et al. 2016), which has a short signal and well-established public posteriors. We analyse the public GW150914 strain data and PSDs from the LVK GWTC-2.1 Zenodo deposit (LIGO Scientific Collaboration & Virgo Collaboration 2022) with IMRPhenomXPHM, using the same heterodyned sampler as for GW170817 with phase marginalisation,³ for this validation run we increase the sampler settings to $n_{\text{live}} = 8000$ with $n_{\text{mcmc}} = 160$ slice steps per update,

LALSUITE reference implementation will be characterised in Chan et al. (2026).

³ Phase marginalisation is not formally valid for a precessing, higher-multipole waveform such as IMRPhenomXPHM, because higher-order modes break the single overall-phase dependence that analytic phase marginalisation assumes. We retain it here for consistency with the GW170817 configuration; the agreement with the published LVK PE –

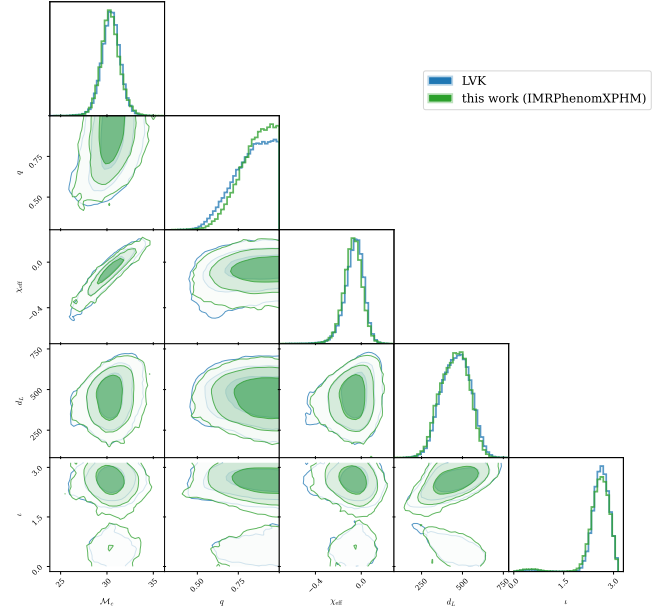


Figure 1. GW150914 validation: corner overlay of the LVK GWTC-2.1 IMRPhenomXPHM posterior (Abbott et al. 2024; LIGO Scientific Collaboration & Virgo Collaboration 2022) and our heterodyned IMRPhenomXPHM run at $n_{\text{live}} = 8000$, $n_{\text{mcmc}} = 160$. The two posteriors overlap throughout the recovered support; our component-mass prior $[5, 100] M_{\odot}$ encompasses the LVK $[10, 80] M_{\odot}$ range without adding posterior mass at the boundaries.

so that the comparison is not sampler-limited at the short-signal n_{dim} . Table 2 compares our recovered parameters with the LVK GWTC-2.1 public PE (Abbott et al. 2024; LIGO Scientific Collaboration & Virgo Collaboration 2022); the corresponding corner overlay is shown in Figure 1. The chirp mass, mass ratio, luminosity distance, and inclination all agree with the LVK reference; in particular, the recovered chirp mass agrees to $\sim 0.2\%$ ($M_c = 30.35$ vs $30.4 M_{\odot}$) and $d_L^{\text{med}} = 455 \text{ Mpc}$ for our IMRPhenomXPHM run is within $\sim 8 \text{ Mpc}$ of the LVK value of 463 Mpc . The 1σ widths match closely: $\sigma(M_c) = 1.02$ vs $1.00 M_{\odot}$, $\sigma(d_L) = 84$ vs 85 Mpc , $\sigma(q) = 0.10$ vs 0.11 , and $\sigma(i) = 0.41$ vs 0.35 rad (ratios 1.02, 0.99, 0.89, 1.17); the largest residual is on the precession-sensitive i . We use a component-mass prior uniform on $[5, 100] M_{\odot}$ that encompasses the LVK GWTC-2.1 $[10, 80] M_{\odot}$ range, with no posterior mass near either boundary; the validation therefore reproduces the LVK posteriors within the recovered support.

3.2 Consistency of the likelihood compression on GW170817

We next verify that the heterodyned (relative-binning) approximation does not bias the GW170817 source-parameter posterior. Relative binning is by now an established compression technique for long-duration binary-neutron-star signals – the DINGO-BNS framework, for example, adopts heterodyning to compress exactly this class of signal (Dax et al. 2025), and rapid approximate analyses are

which does not marginalise over phase – throughout the recovered support (Table 2, Figure 1) confirms it does not measurably bias this validation. The GW170817 science runs use aligned-spin tidal waveforms, for which phase marginalisation is formally valid, so this choice does not affect the H_0 posteriors.

Table 2. GW150914 validation: median values of the principal source parameters for our heterodyned IMRPhenomXPHM run, with a $n_{\text{live}} = 5000$ cross-check. The LVK GWTC-2.1 IMRPhenomXPHM public PE (Abbott et al. 2024; LIGO Scientific Collaboration & Virgo Collaboration 2022) reports $\mathcal{M}_c \approx 30.4 M_\odot$, $q \approx 0.85$, $d_L \approx 463$ Mpc, $\iota \approx 2.62$ rad for direct comparison.

Run	\mathcal{M}_c/M_\odot	q	d_L/Mpc	ι/rad	$\ln Z$
IMRPhenomXPHM ($n_{\text{live}} = 8000$)	30.35	0.87	455	2.61	260.86 ± 0.06
IMRPhenomXPHM ($n_{\text{live}} = 5000$, cross-check)	30.34	0.87	460	2.62	261.09 ± 0.08

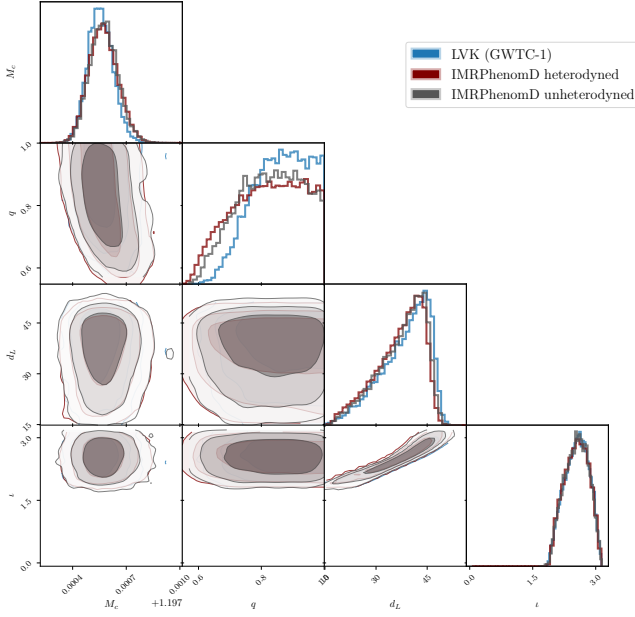


Figure 2. Heterodyned vs full-resolution consistency for GW170817 under IMRPhenomD_NRTidalv2 at $n_{\text{live}} = 1500$. Source-parameter corner overlay of the heterodyned (relative-binning) and full-resolution (full 259 201-bin) posteriors, with the public GWTC-1 IMRPhenomPv2_NRTidal posterior (Abbott et al. 2019b; LIGO Scientific Collaboration & Virgo Collaboration 2018) shown for reference. The heterodyned and full-resolution (\mathcal{M}_c , q , d_L , ι) contours overlap throughout, confirming that the relative-binning approximation does not bias the source-parameter posterior at the level needed for H_0 inference. Two-dimensional marginals are KDE-smoothed.

routine for low-latency alerts – but we confirm it directly for our configuration. We run the same sampler on the full-resolution 259 201-bin frequency-domain likelihood for both IMRPhenomD_NRTidalv2 and TaylorF2 at $n_{\text{live}} = 1500$, and additionally at $n_{\text{live}} \in \{500, 2500\}$ for IMRPhenomD_NRTidalv2. The heterodyned and full-resolution d_L , ι , and H_0 marginals overlay closely (Figure 2), and the heterodyned H_0^{MAP} lies between the surrounding full-resolution cross-checks at the level of the sampler-statistical width. We conclude that the heterodyned approximation is adequate for H_0 inference at this event’s signal-to-noise ratio; the corresponding wall-clock reduction is quantified in Section 5.2.

4 RESULTS

4.1 Prior sensitivity of the GW170817 H_0 posterior

The central scientific result of this paper is a direct comparison between the uniform-in- d_L H_0 posterior obtained by sampling under

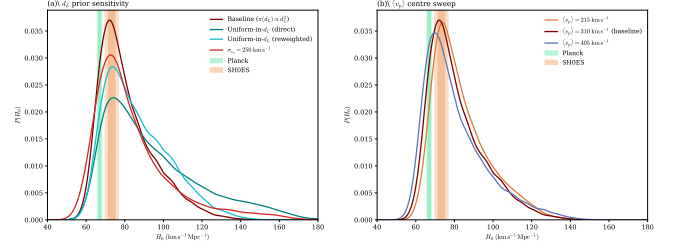


Figure 3. Prior-sensitivity comparison for IMRPhenomXAS_NRTidalv3. *Left panel (a):* kernel-density estimates of the H_0 posterior under the four distance-prior variants of Section 2.4 (volumetric baseline, direct uniform-in- d_L , reweighted uniform-in- d_L , and $\sigma_{v_p} = 250 \text{ km s}^{-1}$). The directly sampled uniform-in- d_L posterior places substantially more mass at high H_0 than the reweighted estimate, despite both targeting the same prior. *Right panel (b):* peculiar-velocity centre sweep — H_0 posteriors for $\langle v_p \rangle \in \{215, 310, 405\} \text{ km s}^{-1}$ at fixed $\sigma_{v_p} = 150 \text{ km s}^{-1}$. Planck Λ CDM and SH0ES distance ladder bands are shown in both panels.

the target prior and that obtained by reweighting the baseline posterior to the same target prior, under the locked primary waveform IMRPhenomXAS_NRTidalv3. We carry out the four prior variants of Section 2.4 on the LVK-matched full-sky prior set and report sample-derived HPDs in Table 3; the corresponding marginals are shown in Figure 3.

4.1.1 Direct-vs-reweighted comparison

The direct uniform-in- d_L run leaves the posterior MAP unchanged at $70.5 \text{ km s}^{-1} \text{ Mpc}^{-1}$ but broadens the 68 per cent HPD on the high side from 87.6 to $103.8 \text{ km s}^{-1} \text{ Mpc}^{-1}$, and raises the high-tail probability

$$P(H_0 > 120 \text{ km s}^{-1} \text{ Mpc}^{-1}) = \begin{cases} 0.017 & (\text{baseline}), \\ 0.159 & (\text{direct uniform-in-}d_L). \end{cases}$$

together with $P(H_0 > 150 \text{ km s}^{-1} \text{ Mpc}^{-1})$ from $< 10^{-4}$ to 0.038 . The reweighted estimate captures a small fraction of this shift: $P(H_0 > 120 \text{ km s}^{-1} \text{ Mpc}^{-1}) = 0.041$, equivalent to

$$\frac{0.041 - 0.017}{0.159 - 0.017} \approx 17\% \quad (3)$$

of the direct prior-induced change. The 68 per cent HPD upper bound under reweighting reaches $95.9 \text{ km s}^{-1} \text{ Mpc}^{-1}$, short of the directly sampled $103.8 \text{ km s}^{-1} \text{ Mpc}^{-1}$ at the same credibility. The reweighted variant is itself consistent with the flat-in-redshift posterior reported by Abbott et al. (2017b) (\approx uniform-in- d_L at this z ; their Extended Data Table 1 gives a 68.3% HPD $H_0 = 71_{-9}^{+23} \text{ km s}^{-1} \text{ Mpc}^{-1}$) – so our reweighting reproduces the original analysis; the deficit we report lies in the directly sampled high- H_0 tail, which the reweighted procedure does not access. The three IMRPhenomXAS_NRTidalv3 prior variants that carry an independent evidence agree to $\Delta \ln Z \lesssim 1.8$; the decision-relevant pair, baseline versus direct uniform-in- d_L ,

Table 3. IMRPhenomXAS_NRTidalv3 H_0 summaries on the LVK-matched full-sky prior set, $n_{\text{live}} = 5000$. Upper block: the four distance-prior variants of Section 2.4 (volumetric baseline, direct and reweighted uniform-in- d_L , and $\sigma_{v_p} = 250 \text{ km s}^{-1}$). Lower block: the peculiar-velocity centre sweep (v_p) $\in \{215, 405\} \text{ km s}^{-1}$ at fixed $\sigma_{v_p} = 150 \text{ km s}^{-1}$ (the $\langle v_p \rangle = 310 \text{ km s}^{-1}$ point is the baseline). MAP, weighted median, and sample-derived 68 per cent HPDs in $\text{km s}^{-1} \text{ Mpc}^{-1}$; the median is reported as a bin-noise-robust complement to the MAP for the skewed posteriors of the uniform-in- d_L variants. The reweighted variant is post-hoc and has no independent $\ln Z$. All numbers generated by `Plots/build_paper_tables.py` from the canonical sample CSVs.

Variant	H_0 ($\text{km s}^{-1} \text{ Mpc}^{-1}$)			$P(H_0 > 120)$	$P(H_0 > 150)$	$\ln Z$
	MAP	median	68% HPD			
Baseline ($\pi(d_L) \propto d_L^2$)	70.5	77.6	[63.8, 87.6]	0.017	$< 10^{-4}$	486.25 ± 0.11
Uniform-in- d_L , direct	70.5	87.6	[64.2, 103.8]	0.159	0.038	487.30 ± 0.10
Uniform-in- d_L , reweighted	73.5	82.9	[65.2, 95.9]	0.041	0.000	(post-hoc)
$\sigma_{v_p} = 250 \text{ km s}^{-1}$	73.5	78.3	[61.7, 90.5]	0.069	0.015	485.55 ± 0.09
$\langle v_p \rangle = 215 \text{ km s}^{-1}$	74.5	79.9	[66.1, 90.4]	0.021	$< 10^{-4}$	485.76 ± 0.12
$\langle v_p \rangle = 405 \text{ km s}^{-1}$	68.5	76.3	[61.5, 87.0]	0.030	0.000	486.35 ± 0.10

differs by only $\Delta \ln Z \approx 1.05$. On the Jeffreys scale this is at most weak-to-substantial support, and it is within the run-to-run variability seen in the public repository for this configuration. The data therefore show at most a weak preference among the distance priors: the change in the high- H_0 tail across these variants is dominated by the *prior*, not by a data-driven update.

4.1.2 Reweighting bias versus variance

The reweighting deficit is bias, not high variance. A non-parametric bootstrap on the reweighted estimator (4000 multinomial-at- n_{eff} draws at the reweighted $n_{\text{eff}} = 27,317$) gives a 95 per cent confidence interval for $P(H_0 > 120 \text{ km s}^{-1} \text{ Mpc}^{-1})$ of [0.037, 0.042] – tight to three significant figures and excluding the directly sampled 0.159 by ~ 100 binomial standard errors of the reweighted estimator. The conclusion is robust to the choice of resampler: a Bayesian (Dirichlet-weighted) bootstrap and a 200-block jack-knife (the standard nonparametric variance estimator for importance-sampling estimators; Owen 2013) both give intervals about 30% wider but with the same centre, and still exclude 0.159 by more than 70 nonparametric standard errors. Down-sampling the baseline to $S \in \{10^4, 3 \times 10^4, 10^5\}$ draws leaves the reweighted point estimate within 0.005 of 0.04 and the bootstrap interval shrinking around 0.04 rather than around 0.159: the reweighted estimator is converging on the wrong limit, not converging slowly. Only direct sampling under the target prior recovers the high- H_0 tail mass. The bootstrap, the sample-size sweep, and the corresponding \hat{k} value below are computed by `analyze_psis_khat.py` in the public repository and recorded in the `paper_diagnostics.csv` summary.

4.1.3 Effective-sample-size diagnostic

The reweighting failure is independently flagged by the effective sample size of the reweighted posterior. We use Kish’s effective sample size, $n_{\text{eff}} = (\sum_i w_i)^2 / \sum_i w_i^2$ (Kish 1965), where w_i are the (nested sampling or importance) weights. From the same 1.73×10^5 -sample IMRPhenomXAS_NRTidalv3 baseline we measure $n_{\text{eff}} = 30,695$ (efficiency 17.8%); the directly sampled uniform-in- d_L run has $n_{\text{eff}} = 37,022$ from its own 1.94×10^5 -sample draw (efficiency 19.1%), while the reweighted uniform-in- d_L estimator has $n_{\text{eff}} = 27,317$ – lower than the baseline despite reweighting from the same draw. The reweighted-versus-baseline comparison is the coverage diagnostic; the directly sampled run is listed for context only, as it has a different sampling history. This is the conventional symptom of importance-sampling weights concentrated on a

small subset of the baseline draw, the regime in which reweighting is known to be unreliable (Payne et al. 2019; Vehtari et al. 2024). The Pareto-smoothed importance-sampling \hat{k} diagnostic of Vehtari et al. (2024), computed by a generalised-Pareto maximum-likelihood fit to the top $M = 3\sqrt{S} = 1,264$ log-importance ratios (the default cap of Vehtari et al. 2024), gives $\hat{k} = 0.683$ for the reweighted IMRPhenomXAS_NRTidalv3 draw: at the upper edge of the cautionary $0.5 < \hat{k} \leq 0.7$ “high variance but consistent” regime, just below the standard $\hat{k} > 0.7$ unreliability threshold.⁴ The empirical bootstrap above shows the bias is already severe at this borderline \hat{k} , so for prior-sensitivity reweighting in the broad-posterior bright-siren regime we recommend reporting a bootstrap confidence interval alongside \hat{k} and n_{eff} . All three diagnostics are cheap, require no additional GPU time, and would have flagged the deficit in the original analysis from the baseline draw alone.

4.1.4 Peculiar-velocity sweep

The $\sigma_{v_p} = 250 \text{ km s}^{-1}$ variant shifts the H_0 posterior modestly: $P(H_0 > 120)$ moves from 0.017 to 0.069. Sweeping the v_p prior centre over the historical literature range $\langle v_p \rangle \in \{215, 310, 405\} \text{ km s}^{-1}$ at fixed $\sigma_{v_p} = 150 \text{ km s}^{-1}$ (Figure 3b, Table 3) shifts H_0^{MAP} by $6 \text{ km s}^{-1} \text{ Mpc}^{-1}$ peak-to-peak (74.5 at $\langle v_p \rangle = 215 \text{ km s}^{-1}$ to 68.5 at $\langle v_p \rangle = 405 \text{ km s}^{-1}$) while $P(H_0 > 120)$ changes by less than 0.02. The $\langle v_p \rangle = 310 \text{ km s}^{-1}$ run replicates the IMRPhenomXAS_NRTidalv3 baseline to within 0.01 in $\ln Z$. For GW170817 with NGC 4993 identified, the dominant prior-induced uncertainty in H_0 is therefore the distance prior, not the peculiar-velocity prior.

4.1.5 Cross-waveform check

Repeating the four-variant prior sweep on the legacy aligned-spin tidal model IMRPhenomD_NRTidalv2 (NRTidalv2 calibration) gives qualitatively the same behaviour with a larger amplitude: baseline $P(H_0 > 120) = 0.076$; uniform-in- d_L direct $P = 0.281$; reweighted $P = 0.195$; reweighting capture fraction $(0.195 - 0.076)/(0.281 - 0.076) \approx 58\%$. The newer NRTidalv3 calibration in IMRPhenomXAS_NRTidalv3 tightens the upper H_0 tail relative to NRTidalv2, leaving less Mode-B mass for the prior

⁴ We cross-checked the local GPD-MLE against the canonical `arviz.psislw` implementation under its PSIS-LOO sign convention, and the two agree to 10^{-3} ($\hat{k}_{\text{arviz}} = 0.683$); the value is also insensitive to the tail-fraction choice within the $M = 3\sqrt{S}$ Vehtari cap.

shift to redistribute and therefore both reducing the absolute prior-induced change in $P(H_0 > 120)$ and reducing the fraction of that change that reweighting can recover. The qualitative conclusion – that reweighting systematically understates the prior-induced change in the high- H_0 tail – is therefore robust across the tidal-calibration axis, and is in fact *more* severe under the modern waveform than under the older one.

The shifts reported here are methodological, not cosmological: GW170817 alone is consistent with both early- and late-Universe H_0 measurements under every prior considered. The point is that the magnitude of this prior-induced change is a property of the inference, and reweighting alone reports a materially smaller value than direct sampling does.

4.2 The d_L - ι bimodality

The uniform-in- d_L posterior is broad and asymmetric, with non-negligible weight at $d_L \lesssim 25$ Mpc. Before isolating the modes quantitatively, we note that the same (d_L, ι) two-peak structure is visible in *both* the IMRX and the IMRPhenomD_NRTidalv2 direct uniform-in- d_L posteriors (Figure 4): the posterior weight in the Mode-B region $d_L < 30$ Mpc is 0.325 under IMRPhenomXAS_NRTidalv3 and 0.428 under IMRPhenomD_NRTidalv2. The bimodality is therefore a property of the data and the uniform-in- d_L prior, not the NRTidalv2 tidal-phase calibration; the reduction in Mode-B weight from IMRPhenomD_NRTidalv2 to IMRPhenomXAS_NRTidalv3 is consistent with the tighter upper H_0 tail under NRTidalv3 reported in Section 4.1. The mode-isolated runs that follow use IMRPhenomD_NRTidalv2/NRTidalv2 at $n_{\text{live}} = 5000$; the cross-waveform check above shows the bimodality is robust to the tidal calibration, so the mode-isolated Bayes factor on IMRPhenomD_NRTidalv2 characterises the same structure that drives the IMRPhenomXAS_NRTidalv3 reweighting deficit reported in Section 4.1.

To resolve whether the IMRPhenomD_NRTidalv2 mode structure is a single broadened mode or a genuine bimodality, we run two prior-restricted variants of the direct uniform-in- d_L analysis: a Mode-A run with $d_L \in [30, 75]$ Mpc and a Mode-B run with $d_L \in [10, 30]$ Mpc. The $d_L = 30$ Mpc split is placed at the approximate saddle separating the two maxima in the joint (d_L, ι) posterior (Figure 5). We retain the original GWTC-1 heterodyne reference, and additionally run an unrestricted $d_L \in [10, 75]$ Mpc uniform-in- d_L analysis with the heterodyne reference re-anchored at Mode B ($d_L = 20$ Mpc, $\iota = 2.0$ rad) to test whether the apparent Mode-B mass is a heterodyne-reference artefact.

Figure 5 shows the joint (d_L, ι) posterior under the unrestricted run, together with the per-mode H_0 marginals. The support is a curved arm running from $(d_L, \iota) \approx (15, 1.9)$ Mpc-rad to $(40, 2.7)$ Mpc-rad with two distinct local maxima. Table 4 reports the local evidences and per-mode H_0 summaries.

The Bayes factor between Mode B and Mode A, after correcting for the volume difference between the restricted priors, is

$$\begin{aligned} \ln \mathcal{B}_{B/A} &= (\ln Z_B - \ln Z_A) + \ln(20/45) \\ &= +0.15 - 0.81 = -0.66 \quad (\text{seed}=0). \end{aligned}$$

An independent second-seed replication (Table 4, lower block) gives $+0.91 - 0.81 = +0.10$ (seed=1). The $\ln(20/45)$ term is the log-ratio of the restricted-prior d_L widths; it is the exact volume correction because the prior is uniform in d_L by construction. Both seeds satisfy $|\ln \mathcal{B}_{B/A}| < 1$, placing the result in the “not worth more than a mention” range of the Jeffreys scale. We caution that

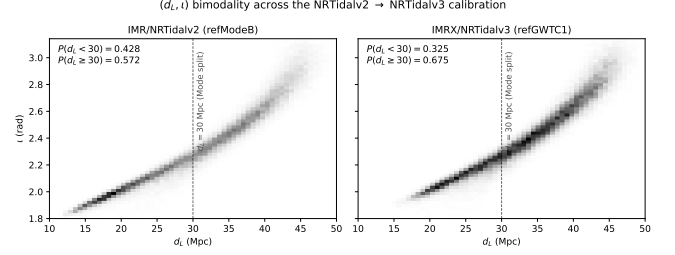


Figure 4. Cross-waveform check on the (d_L, ι) bimodality: weighted joint posteriors from the unrestricted direct uniform-in- d_L runs at IMRPhenomD_NRTidalv2 (left; Mode-B-anchored heterodyne reference) and IMRPhenomXAS_NRTidalv3 (right; default GWTC-1 reference). Both show the same two-peak structure with the Mode-B region $d_L < 30$ Mpc carrying 0.428 (IMRPhenomD_NRTidalv2) and 0.325 (IMRPhenomXAS_NRTidalv3) of the posterior weight: the bimodality is robust across the NRTidalv2 \rightarrow NRTidalv3 calibration. The smaller IMRX Mode-B weight is consistent with the tighter upper H_0 tail under NRTidalv3 reported in Section 4.1.

the run-to-run $\ln Z$ scatter is larger than the nominal ± 0.1 per-run uncertainty: the unrestricted $\ln Z$ differs by 1.04 between the two seeds, so the ± 0.1 figure should be read as a within-run statistical error, not a run-to-run reproducibility bound. This scatter motivates cross-checking the nested sampling evidence against an independent normalising-constant estimator, such as sequential Monte Carlo (Williams et al. 2025), to establish whether it reflects a limitation of the nested sampling evidence estimate or the intrinsic difficulty of this multimodal problem; a larger ensemble of independent repeats would address the same question empirically and is left to follow-up work. The conclusion that survives this scatter is the sign-independent one – $|\ln \mathcal{B}_{B/A}| < 1$ in both seeds – so Mode B is neither significantly favoured nor disfavoured regardless of seed. A larger seed ensemble would tighten this to a distributional rather than sign-only claim; the `analyze_seed_ensemble.py` script in the public data release aggregates seeds as they accumulate. Mode B contributes a non-negligible share of the joint posterior under any prior that gives the low- d_L region appreciable weight. The Mode-B-anchored unrestricted run recovers $P(H_0 > 120) = 0.281$ – statistically indistinguishable from the GWTC-1-anchored IMRPhenomD_NRTidalv2 direct uniform-in- d_L run reported in Section 4.1 – so the heterodyne-reference choice does not bias the Mode-A/Mode-B weight ratio under IMRPhenomD_NRTidalv2/NRTidalv2; the corresponding IMRX mode-isolated set with a Mode-B-anchored reference is queued as follow-up.

This is the mechanism behind the reweighting capture fraction of equation 3. Mode B is the high- H_0 , small- d_L branch of the distance-inclination degeneracy. The baseline volumetric prior $\pi(d_L) \propto d_L^2$ assigns Mode B a tiny prior mass (the $[10, 30]$ Mpc slab carries $(30^3 - 10^3)/(75^3 - 10^3) \approx 6\%$ of the total $[10, 75]$ Mpc volumetric prior), and the corresponding region of the baseline posterior is sparsely sampled. Reweighting cannot reconstruct what is not there. Direct sampling under the uniform-in- d_L prior populates Mode B at sampler resolution, and it is precisely the missing Mode-B mass that opens the gap between the directly sampled and reweighted estimates of $P(H_0 > 120)$. Posterior-coverage diagnostics that compare the baseline samples against the target prior – such as the n_{eff} measurement reported in Section 4.1 – should therefore be standard practice before reporting a reweighted bright-siren H_0 summary.

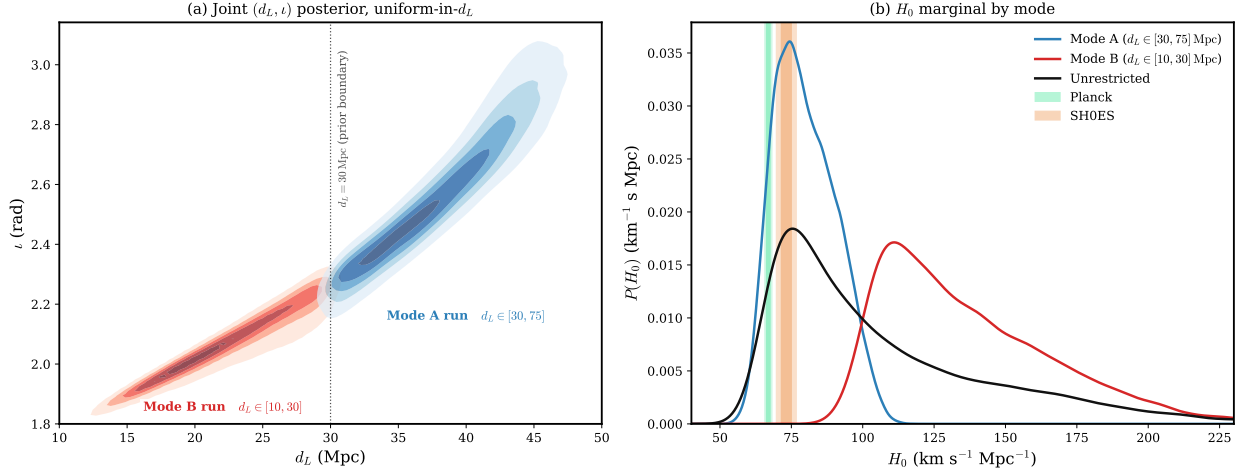


Figure 5. The d_L - t bimodality in the GW170817 uniform-in- d_L posterior. Left: joint (d_L, t) posterior from the unrestricted $d_L \in [10, 75]$ Mpc run (Mode-B-anchored heterodyne reference); the prior-restricted Mode-A and Mode-B contours from the two separate restricted-prior runs are overlaid in distinct colours, with the $d_L = 30$ Mpc prior boundary marked. Right: per-mode H_0 marginals as Silverman-bandwidth kernel-density estimates. The Planck Λ CDM and SH0ES distance ladder bands are shown for context.

Table 4. Local evidences, MAP H_0 values, and sample-derived 68 per cent HPDs for the d_L -restricted uniform-in- d_L runs; the lower block is an independent replication. The Mode-B/Mode-A Bayes factor includes a $\ln(20/45)$ correction for the difference in restricted-prior d_L volumes.

Variant	d_L range (Mpc)	H_0^{MAP} ($\text{km s}^{-1} \text{Mpc}^{-1}$)	68% HPD	$P(H_0 > 120)$	$\ln Z$
Mode A	[30, 75]	74.5	[66.7, 88.8]	$< 10^{-4}$	486.80 ± 0.10
Mode B	[10, 30]	109.5	[99.5, 151.8]	0.638	486.95 ± 0.09
Unrestricted	[10, 75]	73.5	[62.6, 116.5]	0.281	486.48 ± 0.09
Mode A	[30, 75]	72.5	[66.1, 88.6]	$< 10^{-4}$	486.71 ± 0.09
Mode B	[10, 30]	110.5	[99.0, 154.5]	0.646	487.62 ± 0.10
Unrestricted	[10, 75]	73.5	[62.0, 121.1]	0.311	487.52 ± 0.09

4.3 Cross-waveform Hubble-constant posterior

Figure 6 shows the GW170817 H_0 posterior under the LVK-matched prior (Section 2.4) for IMRPhenomXAS_NRTidalv3 and TaylorF2, together with the Planck and SH0ES reference bands. The plotted curves are Silverman-bandwidth kernel-density estimates; the sample-derived HPDs (computed from the weighted samples, no KDE) are reported in Table 5. Figure 7 shows the corresponding $(\mathcal{M}_c, q, \chi_{\text{eff}}, d_L, t)$ corner overlay against the public GWTC-1 IMRPhenomPv2_NRTidal posterior (Abbott et al. 2019b; LIGO Scientific Collaboration & Virgo Collaboration 2018).

IMRPhenomXAS_NRTidalv3, the locked primary, has $H_0^{\text{MAP}} = 70.5 \text{ km s}^{-1} \text{Mpc}^{-1}$, 68 per cent HPD $[63.8, 87.6] \text{ km s}^{-1} \text{Mpc}^{-1}$ and 95 per cent HPD $[59.3, 112.4] \text{ km s}^{-1} \text{Mpc}^{-1}$; this is the baseline run of Section 4.1 (Table 3), reused here as the reference waveform for the cross-waveform comparison. TaylorF2, a post-Newtonian inspiral-only family check on the same prior, has $H_0^{\text{MAP}} = 68.5 \text{ km s}^{-1} \text{Mpc}^{-1} - \sim 2 \text{ km s}^{-1} \text{Mpc}^{-1}$ lower, the small offset expected for a lower-PN, point-particle inspiral family – and 68 per cent HPD $[61.2, 89.3] \text{ km s}^{-1} \text{Mpc}^{-1}$, overlapping IMRPhenomXAS_NRTidalv3 throughout. The published Abbott+2017 result $H_0 = 70_{-8}^{+12} \text{ km s}^{-1} \text{Mpc}^{-1}$ (Abbott et al. 2017b) is consistent with both. TaylorF2 carries the heavier upper tail (95 per cent upper bound 127.0 versus 112.4 $\text{km s}^{-1} \text{Mpc}^{-1}$ for IMRPhenomXAS_NRTidalv3, and $P(H_0 > 120) = 0.065$ versus 0.017), which we attribute to the more recent NR-calibrated tides in IMRPhenomXAS_NRTidalv3 damping the high- H_0 , small- d_L branch of the degeneracy. The

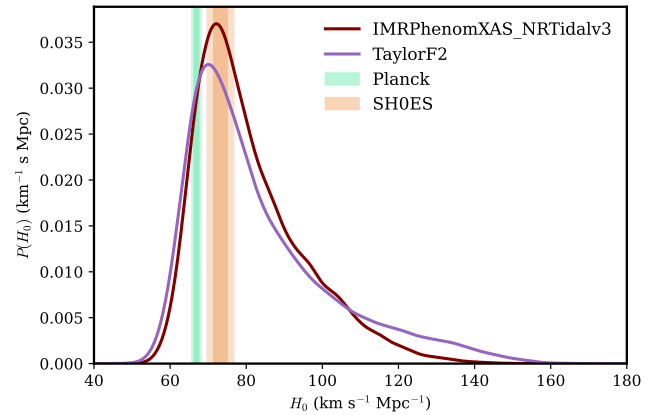


Figure 6. GW170817 H_0 posterior for IMRPhenomXAS_NRTidalv3 and TaylorF2 on the LVK-matched prior, shown as Silverman-bandwidth kernel-density estimates; the sample-derived 68 and 95 per cent HPDs (computed from the weighted samples, no KDE) are reported in Table 5. The Planck Λ CDM and SH0ES distance ladder values are shown for context.

IMRX-vs-IMR capture-fraction comparison reported in Section 4.1 indicates that the same tide-driven tail compression accounts for the smaller absolute prior-induced shift in $P(H_0 > 120)$ under IMRPhenomXAS_NRTidalv3.

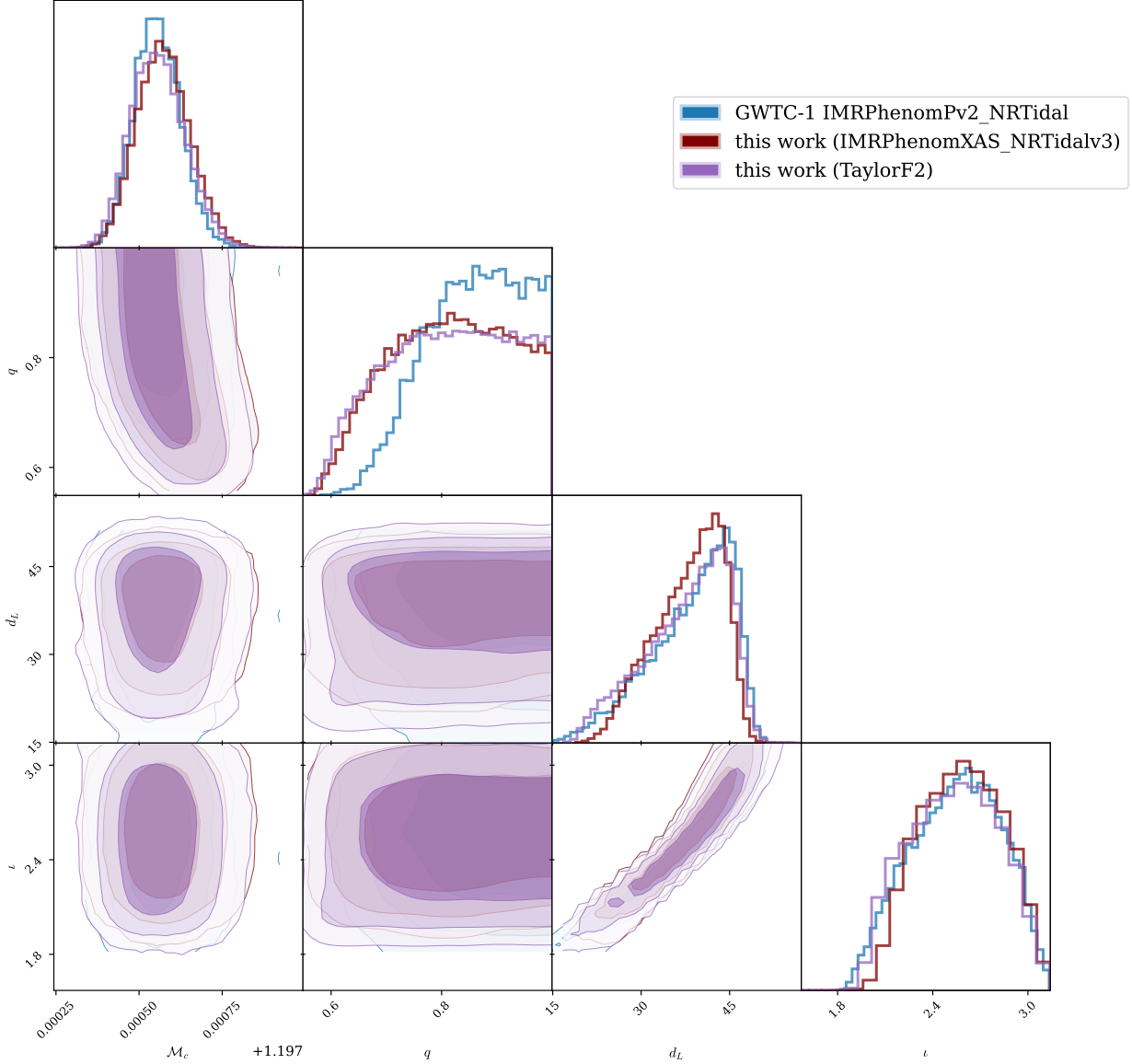


Figure 7. GW170817 source-parameter corner overlay for IMRPhenomXAS_NRTidalv3 and TaylorF2 on the LVK-matched prior, with the public GWTC-1 IMRPhenomPv2_NRTidal posterior (Abbott et al. 2019b; LIGO Scientific Collaboration & Virgo Collaboration 2018) included as a literature reference. Two-dimensional contours and one-dimensional marginals are KDE-smoothed.

Table 5. GW170817 H_0 summaries for the two-waveform main set on the LVK-matched prior, $n_{\text{live}} = 5000$. MAP and sample-derived HPDs in $\text{km s}^{-1} \text{Mpc}^{-1}$. The IMRPhenomXAS_NRTidalv3 row is the baseline run of Table 3.

Waveform	MAP	68% HPD	95% HPD	$P(H_0 > 120)$	$\ln Z$
IMRPhenomXAS_NRTidalv3	70.5	[63.8, 87.6]	[59.3, 112.4]	0.017	486.25 ± 0.11
TaylorF2	68.5	[61.2, 89.3]	[56.7, 127.0]	0.065	486.90 ± 0.10

5 PERFORMANCE AND RUNTIME STUDIES

5.1 Wall-clock runtime

The primary heterodyned GW170817 H_0 analysis with IMRPhenomXAS_NRTidalv3 and $n_{\text{live}} = 5000$ on the LVK-matched prior set completes in ≈ 13 min on a single NVIDIA A100 40 GB SXM4 GPU (Google Cloud a2-highgpu-1g class); the corresponding TaylorF2 run takes ≈ 4 min. This wall-clock is comparable per

live point to other JAX-based BNS pipelines (Wong et al. 2023; Wouters et al. 2024) on similar hardware. The full four-variant prior-sensitivity suite (baseline, direct uniform-in- d_L , reweighted post-hoc, $\sigma_{v_p} = 250 \text{ km s}^{-1}$) for IMRPhenomXAS_NRTidalv3 on the LVK-matched prior set fits inside an hour. The GW150914 IMRPhenomXPHM validation run at the larger $n_{\text{live}} = 8000$, $n_{\text{mcmc}} = 160$ settings takes ≈ 5 h on the same hardware – the price for the converged short-signal sampler configuration that yields the LVK reproduction

of Section 3.1 together with the JAX RIPPLE IMRPhenomXPHM implementation (Edwards et al. 2024), which, unlike the aligned-spin tidal waveforms used for the GW170817 science runs, is not yet performance-optimised; we expect this wall-clock to fall substantially once that implementation is optimised.

5.2 Heterodyne speedup and live-point scaling

The heterodyned (relative-binning) likelihood is the enabling approximation: at matched live-point count it runs $\sim 50\times$ faster than the full-resolution reference, averaged over $n_{\text{live}} = 500\text{--}2500$, with the relative-binning approximation accounting for the bulk of the reduction and the GPU saturation provided by BLACKJAX-NS layered on top. The heterodyned H_0^{MAP} is stable across $n_{\text{live}} \geq 2500$ to within $1 \text{ km s}^{-1} \text{ Mpc}^{-1}$ and $\ln Z$ to within ± 0.2 over the same range, so the $n_{\text{live}} = 5000$ configuration adopted for the science runs sits in the converged regime; live-point counts up to 10^5 remain accessible on a single GPU, with the $n_{\text{live}} = 10^5$ heterodyned run completing in roughly four hours. The full live-point scaling characterisation of a closely related BLACKJAX-NS nested sampling pipeline is reported by Prathaban et al. (2026); the GW170817-specific timings underlying the speedup quoted here are tabulated in Results/scaling_study/scaling_summary_full.csv in the public data release.

5.3 Scope of the performance claim

The runtime numbers above are single-A100 wall-clock on the current pipeline: the full $n_{\text{live}} = 5000 H_0$ analysis completes in under a quarter of an hour, the multi-variant prior-sensitivity suite fits inside an hour, and the live-point convergence study extends to $n_{\text{live}} = 10^5$ within an overnight budget. This budget is what makes the multi-axis robustness study of this paper scientifically routine. A like-for-like IMRPhenomXAS_NRTidalv3 PARALLEL_BILBY benchmark on matched priors and live-point counts would calibrate the speedup against a production CPU pipeline and is the appropriate cross-check for a follow-up.

6 DISCUSSION

6.1 Implications for bright-siren cosmology

The main methodological message is that posterior reweighting, although statistically consistent in the limit of infinite baseline samples, can substantially understate the prior sensitivity of bright-siren H_0 measurements in practice. For GW170817 under IMRPhenomXAS_NRTidalv3, switching from a volumetric distance prior to a uniform-in- d_L prior changes $P(H_0 > 120 \text{ km s}^{-1} \text{ Mpc}^{-1})$ by a factor of ≈ 9 under direct sampling, while reweighting captures only $\approx 17\%$ of that shift (equation 3). The corresponding capture fraction on IMRPhenomD_NRTidalv2 – where the high- H_0 tail is heavier – rises to $\approx 58\%$. The deficit is a problem of effective sample coverage rather than of statistical methodology: the baseline volumetric prior assigns Mode B a small prior mass and reweighting cannot reconstruct what was not sampled. The reweighted posterior’s effective sample size, lower than the baseline’s despite reweighting from the same draw, independently flags the coverage failure and is the diagnostic we recommend as a default check before any reweighted bright-siren H_0 summary is reported.

For a single event the cosmological interpretation is robust to this under-estimation: both early- and late-Universe H_0 values lie within

the GW170817 68 per cent HPD under any of the priors considered here. However, the scale of the effect matters for forecasts (Chen et al. 2018) and combined analyses. When bright-siren posteriors are combined over multiple events, or when tail probabilities are compared against external priors from cosmological surveys, the prior-dependence of each single-event posterior propagates through. An analysis that quantifies that dependence through reweighting alone will systematically underestimate the prior contribution.

6.2 Where reweighting is sufficient

Reweighting is adequate when the target and baseline priors have similar support in the regions that carry most of the posterior mass. The $\sigma_{v_p} = 250 \text{ km s}^{-1}$ variant in our analysis is a case of this kind: the change modifies the host-velocity likelihood smoothly over the scale of the velocity posterior, the baseline samples cover the affected region well, and the reweighted and directly sampled σ_{v_p} posteriors agree to well within the statistical width. The uniform-in- d_L case fails the same coverage test, because the baseline volumetric and target uniform-in- d_L priors differ most at the edges of the d_L range. The mode-isolated runs of Section 4.2 make this concrete: Mode B has $|\ln \mathcal{B}_{B/A}| < 1$ relative to Mode A (confirmed over two independent seeds) under the uniform-in- d_L prior, but its baseline-volumetric-prior mass is only $\approx 7\%$ of Mode A’s, so reweighted samples are blind to it.

6.3 Implications for future bright sirens

The practical consequence is that direct prior sampling should be used for bright-siren H_0 analyses whenever the target prior differs non-trivially in support from the baseline, rather than being used only as a cross-check. The runtime budget on a single A100 GPU now permits such reruns routinely (Section 5); the live-point and sampler-robustness studies (Appendix A) show that the science-quality configuration sits in the converged regime, so the marginal cost of such a rerun is the marginal cost of one ~ 15 min run. Live-point counts up to 10^5 are accessible on the same hardware, which means that these studies can be combined with population-level analyses without a substantial increase in end-to-end wall-clock time. This is directly relevant to the third-generation detector era, where the detection rate of compact-binary mergers will make repeated, controlled posterior reanalyses the norm rather than the exception. Quantitatively, Chen et al. (2018) project of order 25–80 bright-siren events with electromagnetic counterparts within 5–10 years from a network including A+ LIGO and Voyager, with per-event posterior widths comparable to GW170817’s; for the Einstein Telescope and Cosmic Explorer era, the projected compact-binary detection rate brings the bright-siren sub-population to of order tens to hundreds per year (e.g. Branchesi et al. 2023), a regime in which the per-event parameter-estimation cost itself becomes a bottleneck (Hu & Veitch 2025). At the $\lesssim 15$ min-per-event runtime reported in Section 5 this makes per-event prior-sensitivity reruns routine across that population. For comparison-grade single-event posteriors we recommend reporting both the volumetric (which coincides with the comoving-volume prior at $z \lesssim 0.02$) and the uniform-in- d_L direct-sampled posteriors; the difference between the two bounds the prior-induced systematic.

7 CONCLUSIONS

We have used a GPU-native nested sampling pipeline to revisit the GW170817 bright-siren H_0 measurement of Abbott et al. (2017b). Switching the distance prior from volumetric to uniform-in- d_L by direct sampling raises $P(H_0 > 120 \text{ km s}^{-1} \text{ Mpc}^{-1})$ from 0.017 to 0.159 and moves the weighted-median H_0 from 77.6 to 87.6 $\text{km s}^{-1} \text{ Mpc}^{-1}$, while the binned MAP stays at 70.5 $\text{km s}^{-1} \text{ Mpc}^{-1}$; post-hoc reweighting captures only 0.041 in the tail, $\approx 17\%$ of the directly sampled shift. The three IMRPhenomXAS_NRTidalv3 prior variants that carry an independent evidence agree to $\Delta \ln Z \lesssim 1.8$, so the tail and bulk shifts are properties of the prior, not data updates. The mechanism is the d_L - t bimodality: a high- H_0 , small- d_L branch (Mode B; $|\ln \mathcal{B}_{B/A}| < 1$, confirmed in two independent seeds) carries appreciable likelihood but negligible volumetric-prior mass, and reweighting cannot recover what was not sampled. The reweighted estimator's effective sample size, lower than the baseline's, independently flags the coverage failure. The runtime budget makes direct prior-sensitivity reruns the right default for bright-siren cosmology, with multi-axis robustness studies now routine on a single A100 GPU. Methodologically, the runtime budget delivered by the GPU-native Nested Slice Sampling pipeline is what turns a systematic, multi-axis prior-sensitivity study from a major undertaking into a routine one, and we expect fast differentiable pipelines of this kind to make such studies standard in bright-siren cosmology.

Two natural extensions sit outside the scope of the present analysis. First, no waveform in our JAX inventory simultaneously includes precession and tides, so the locked primary is the aligned-spin tidal IMRPhenomXAS_NRTidalv3; a tides-with-precession waveform in JAX would extend the cross-waveform check. Second, the d_L - t bimodality is characterised here at the level of local evidences and mode-isolated marginals; propagating Mode B into a population analysis, or combining it with an electromagnetic likelihood for the host inclination, is the natural next step for bright-siren cosmology built on this finding.

ACKNOWLEDGEMENTS

This work was supported by the research environment and infrastructure of the Handley Lab at the University of Cambridge. This material is based upon work supported by the Google Cloud research credits program, with the award GCP397499138. We acknowledge the LIGO–Virgo–KAGRA Collaboration for the public strain data and reference posteriors used here (Abbott et al. 2019b, 2024; LIGO Scientific Collaboration & Virgo Collaboration 2018, 2017, 2022).

DATA AVAILABILITY

The GW170817 strain data, host-galaxy peculiar-velocity inputs, and GWTC-1 reference posteriors used here are from the LIGO–Virgo Collaboration data releases LIGO P1800061 and P1700296 (LIGO Scientific Collaboration & Virgo Collaboration 2018, 2017). The GW150914 strain data and the GWTC-2.1 IMRPhenomXPHM reference parameter-estimation posterior are from the LVK GWTC-2.1 Zenodo deposit (LIGO Scientific Collaboration & Virgo Collaboration 2022). The analysis scripts, derived summary tables, run catalogue, and figure- and table-generation code needed to reproduce the results in this paper can be obtained from Yang et al. (2026). The nested sampling chains themselves are not redistributed in that repository (each individual chain is ~ 100 MB and the full set runs to several GB); they can be regenerated from the public strain data using

the BLACKJAX-NS nested slice sampling kernel (Yallup et al. 2026); the broader GW-analysis tooling and example scripts of Prathanan et al. (2026) provide instructions for running GW analyses of this kind.

REFERENCES

- Abac A., Dietrich T., Buonanno A., Steinhoff J., Ujevic M., 2024, *Physical Review D*, 109, 024062
- Abbott B. P., et al., 2016, *Physical Review Letters*, 116, 061102
- Abbott B. P., et al., 2017a, *Physical Review Letters*, 119, 161101
- Abbott B. P., et al., 2017b, *Nature*, 551, 85
- Abbott B. P., et al., 2019a, *Physical Review X*, 9, 011001
- Abbott B. P., et al., 2019b, *Physical Review X*, 9, 031040
- Abbott B. P., et al., 2020, *Living Reviews in Relativity*, 23, 3
- Abbott R., et al., 2024, *Physical Review D*, 109, 022001
- Ashton G., 2026, *RAS Techniques and Instruments*, 5, rzag012
- Ashton G., et al., 2019, *The Astrophysical Journal Supplement Series*, 241, 27
- Bradbury J., et al., 2018, JAX: composable transformations of Python+NumPy programs, <https://github.com/google/jax>
- Branchesi M., et al., 2023, *Journal of Cosmology and Astroparticle Physics*, 2023, 068
- Cabezas A., Corenflos A., Lao J., Louf R., et al., 2024, BlackJAX: Composable Bayesian inference in JAX ([arXiv:2402.10797](https://arxiv.org/abs/2402.10797))
- Chan R., Narola H., Ng T. C. K., Wouters T., Wong I. C. F., Gittins F., Janquart J., Van Den Broeck C., 2026, in prep.
- Chen H.-Y., Fishbach M., Holz D. E., 2018, *Nature*, 562, 545
- Cornish N. J., 2010, Fast Fisher Matrices and Lazy Likelihoods ([arXiv:1007.4820](https://arxiv.org/abs/1007.4820))
- Dax M., et al., 2025, *Nature*, 639, 49
- Di Valentino E., et al., 2021, *Classical and Quantum Gravity*, 38, 153001
- Edwards T. D. P., Wong K. W. K., Lam K. K. H., Coogan A., Foreman-Mackey D., Isi M., Zimmerman A., 2024, *Physical Review D*, 110, 064028
- Finn L. S., Chernoff D. F., 1993, *Phys. Rev. D*, 47, 2198
- Holz D. E., Hughes S. A., 2005, *The Astrophysical Journal*, 629, 15
- Hotokezaka K., Nakar E., Gottlieb O., Nissanke S., Masuda K., Hallinan G., Mooley K. P., Deller A. T., 2019, *Nature Astronomy*, 3, 940
- Howlett C., Davis T. M., 2020, *Monthly Notices of the Royal Astronomical Society*, 492, 3803
- Hu Q., Veitch J., 2025, *Physical Review D*, 112, 084039
- Kish L., 1965, Survey Sampling. John Wiley & Sons, New York
- Krishna K., Vijaykumar A., Ganguly A., Talbot C., Biscoveanu S., George R. N., Williams N., Zimmerman A., 2023, Accelerated parameter estimation in Bilby with relative binning ([arXiv:2312.06009](https://arxiv.org/abs/2312.06009))
- LIGO Scientific Collaboration Virgo Collaboration 2017, A gravitational-wave standard siren measurement of the Hubble constant – Data Release, LIGO Document P1700296; <https://dcc.ligo.org/LIGO-P1700296/public>
- LIGO Scientific Collaboration Virgo Collaboration 2018, Properties of the binary neutron star merger GW170817 – Data Release, LIGO Document P1800061; <https://dcc.ligo.org/LIGO-P1800061/public>
- LIGO Scientific Collaboration Virgo Collaboration 2022, GWTC-2.1: Deep Extended Catalog of Compact Binary Coalescences Observed by LIGO and Virgo During the First Half of the Third Observing Run – Parameter Estimation Data Release, Zenodo, <https://doi.org/10.5281/zenodo.6513631>, doi:10.5281/zenodo.6513631
- LIGO Scientific Collaboration Virgo Collaboration KAGRA Collaboration 2026, GWTC-5.0: Constraints on the Cosmic Expansion Rate and Modified Gravitational-wave Propagation ([arXiv:2605.27227](https://arxiv.org/abs/2605.27227)), doi:10.48550/arXiv.2605.27227
- Mooley K. P., et al., 2018, *Nature*, 561, 355
- Morisaki S., 2021, *Physical Review D*, 104, 044062
- Mukherjee S., Lavaux G., Bouchet F. R., Jasche J., Wandelt B. D., Nissanke S., Leclercq F., Hotokezaka K., 2021, *Astronomy and Astrophysics*, 646, A65

Nicolaou C., Lahav O., Lemos P., Hartley W., Braden J., 2020, *Monthly Notices of the Royal Astronomical Society*, 495, 90

Owen A. B., 2013, Monte Carlo Theory, Methods and Examples, <https://artowen.su.domains/mc/>

Palmese A., Mastrogiovanni S., 2025, Gravitational Wave Cosmology ([arXiv:2502.00239](https://arxiv.org/abs/2502.00239))

Palmese A., Kaur R., Hajela A., Margutti R., McDowell A., MacFadyen A., 2024, *Physical Review D*, 109, 063508

Payne E., Talbot C., Thrane E., 2019, *Physical Review D*, 100, 123017

Planck Collaboration 2020, *Astronomy and Astrophysics*, 641, A6

Prathaban M., Yallup D., Alvey J., Yang M. H., Templeton W., Handley W., 2026, *RAS Techniques and Instruments*, 5, rzag034

Pratten G., Husa S., García-Quirós C., Colleoni M., Ramos-Buades A., Estellés H., Jaume R., 2020, *Physical Review D*, 102, 064001

Pratten G., et al., 2021, *Physical Review D*, 103, 104056

Riess A. G., et al., 2016, *The Astrophysical Journal*, 826, 56

Riess A. G., et al., 2022, *The Astrophysical Journal Letters*, 934, L7

Salvarese A., Chen H.-Y., 2024, *The Astrophysical Journal Letters*, 974, L16

Schutz B. F., 1986, *Nature*, 323, 310

Skilling J., 2006, *Bayesian Analysis*, 1, 833

Smith R., Field S. E., Blackburn K., Haster C.-J., Pürrer M., Raymond V., Schmidt P., 2016, *Physical Review D*, 94, 044031

Speagle J. S., 2020, *Monthly Notices of the Royal Astronomical Society*, 493, 3132

Vehtari A., Simpson D., Gelman A., Yao Y., Gabry J., 2024, *Journal of Machine Learning Research*, 25, 1

Vinciguerra S., Veitch J., Mandel I., 2017, *Classical and Quantum Gravity*, 34, 115006

Wang Y.-Y., Tang S.-P., Jin Z.-P., Fan Y.-Z., 2023, *The Astrophysical Journal*, 943, 13

Williams M. J., Veitch J., Messenger C., 2021, *Physical Review D*, 103, 103006

Williams M. J., Karamanis M., Luo Y., Seljak U., 2025, *Monthly Notices of the Royal Astronomical Society*, 543, 1479

Wong K. W. K., Isi M., Edwards T. D. P., 2023, *The Astrophysical Journal*, 958, 129

Wouters T., Pang P. T. H., Dietrich T., Van Den Broeck C., 2024, *Physical Review D*, 110, 083033

Yallup D., Prathaban M., Alvey J., Handley W., 2025, Parallel Nested Slice Sampling for Gravitational Wave Parameter Estimation ([arXiv:2509.24949](https://arxiv.org/abs/2509.24949))

Yallup D., Kroupa N., Handley W., 2026, *Transactions on Machine Learning Research*

Yang M. H., Prathaban M., Yallup D., Handley W., 2026, GW170817 bright-siren H_0 : data and analysis release, <https://github.com/ming-256/GW170817-bright-siren-H0>, doi:10.5281/zenodo.21038511

Zackay B., Dai L., Venumadhav T., 2018, Relative binning and fast likelihood evaluation for gravitational-wave parameter estimation ([arXiv:1806.08792](https://arxiv.org/abs/1806.08792))

APPENDIX A: INLINE ROBUSTNESS SWEEPS

We complete the multi-axis robustness picture with sweeps held in this appendix; the prior-sensitivity result of Section 4.1 survives every one of them.

Sampler hyperparameters. On the IMRPhenomD_NRTidalv2 LVK-matched baseline at $n_{\text{live}} = 5000$, varying $n_{\text{delete}}/n_{\text{live}} \in \{0.10, 0.25, 0.50, 0.75\}$ moves H_0^{MAP} by $\leq 1.2 \text{ km s}^{-1} \text{ Mpc}^{-1}$ and $\ln Z$ by ≤ 0.6 ; varying the heterodyne-bin count $n_{\text{bins}} \in \{251, 501, 1001\}$ moves H_0^{MAP} by $\leq 0.7 \text{ km s}^{-1} \text{ Mpc}^{-1}$, with the largest pairwise Wasserstein-1 distance between the three H_0 posteriors below $2 \text{ km s}^{-1} \text{ Mpc}^{-1}$.

PSD source. TaylorF2 runs at $n_{\text{live}} = 5000$ on the baseline prior with GWTC-1, kazewong, and BILBY reference PSDs span $H_0^{\text{MAP}} =$

Table A1. IMRPhenomD_NRTidalv2 companion four-variant prior-sensitivity sweep, the legacy-waveform analogue of Table 3. MAP in $\text{km s}^{-1} \text{ Mpc}^{-1}$.

Variant	H_0^{MAP}	$P(H_0 > 120)$
Volumetric baseline	71.5	0.076
Uniform-in- d_L (direct)	73.5	0.281
Uniform-in- d_L (reweighted)	71.5	0.195
$\sigma_{v_p} = 250 \text{ km s}^{-1}$	70.5	0.067

$76.4\text{--}77.7 \text{ km s}^{-1} \text{ Mpc}^{-1}$ and $P(H_0 > 120) = 0.043\text{--}0.065$, again with maximum pairwise $W_1 < 2 \text{ km s}^{-1} \text{ Mpc}^{-1}$.

Heterodyne reference. Replacing the GWTC-1 reference parameters with an optimised (maximum-likelihood) reference point from an initial low-cost optimisation produces IMRPhenomD_NRTidalv2 posteriors that are indistinguishable through the bulk of the distribution and depart only in the high- H_0 tail.

Peculiar-velocity centre. Sweeping $\langle v_p \rangle \in \{215, 310, 405\} \text{ km s}^{-1}$ at fixed $\sigma_{v_p} = 150 \text{ km s}^{-1}$ on the IMRPhenomXAS_NRTidalv3 baseline (Figure 3b, Table 3) shifts H_0^{MAP} by $6 \text{ km s}^{-1} \text{ Mpc}^{-1}$ peak-to-peak across the full range (74.5 at $\langle v_p \rangle = 215 \text{ km s}^{-1}$ to 68.5 at $\langle v_p \rangle = 405 \text{ km s}^{-1}$), while $P(H_0 > 120)$ changes by less than 0.02. The $\langle v_p \rangle = 310 \text{ km s}^{-1}$ run reproduces the IMRPhenomXAS_NRTidalv3 baseline to within 0.01 in $\ln Z$, confirming run reproducibility.

IMRPhenomD_NRTidalv2 companion full sweep. The four-variant prior-sensitivity sweep on IMRPhenomD_NRTidalv2 (Table A1) reproduces the IMRPhenomXAS_NRTidalv3 behaviour with a larger amplitude: the reweighting-capture fraction is $(0.195 - 0.076)/(0.281 - 0.076) \approx 58\%$, against $\approx 17\%$ for IMRPhenomXAS_NRTidalv3 (equation 3).

All five axes therefore produce H_0 shifts at least an order of magnitude smaller than the prior-induced shift documented in Section 4.1.